Drag reduction assisted emulsification in a micro-channel

Elia Missi, Agnès Montillet, Jérôme Bellettre, Teodor Burghelea

Nantes Université, CNRS, Laboratoire de Thermique et Energie de Nantes, UMR 6607, La Chantrerie, Rue Christian Pauc, B.P. 50609, F-44306 Nantes Cedex 3, France

Graphical Abstract

Drag reduction assisted emulsification in a micro-channel

Elia Missi, Agnès Montillet, Jérôme Bellettre, Teodor Burghelea

Highlights

Drag reduction assisted emulsification in a micro-channel

Elia Missi, Agnès Montillet, Jérôme Bellettre, Teodor Burghelea

- Emulsification can be efficiently assisted by the drag reduction
- The addition of xanthan gum significantly enriches the panorama of dispersion modes

Drag reduction assisted emulsification in a micro-channel

Elia Missi[a], Agnès Montillet[b], Jérôme Bellettre[a], Teodor Burghelea[a]

[a] *Laboratoire de Thermique et Enérgie de Nantes, CNRS, Nantes Université, Rue Christian Pauc, B.P. 50609, Nantes, 44306, France*
[b] *Nantes Université , Oniris, CNRS, GEPEA, UMR 6144, CRTT - 37 Bd Université - CS 90406, Saint Nazaire, F-44600, France*

Abstract

An experimental study of the turbulent dynamics of emulsification in a cross-slot microfluidic device is presented. The continuous phase contains a minute amount of an inelastic polymer (xanthan). The Reynolds numbers are sufficiently large (up to 16000) so the drag reduction phenomenon is observed during the emulsification process. The statistics of droplet sizes in the resulting emulsions are measured ex-situ by means of digital microscopy in a wide range of Reynolds numbers and polymer concentrations in the continuous phase. Integral measurements of the statistics of the pressure drops in the micro-channel allow one to systematically map the drag reduction states. Corresponding to each state, the space-time dynamics of the emulsification process are assessed by means of in-situ high speed imaging of the interface between the two fluids which further allows one to extract the characteristic time and space scales associated to the dynamics of the interface. Various dynamic regimes of the microscopic emulsification process are mapped in terms of the Reynolds number and shear thinning rheology of the continuous phase.

Keywords: emulsification, drag reduction, turbulent flow, microfluidics
PACS: 0000, 1111
2000 MSC: 0000, 1111

1. Introduction

High throughput emulsification is important for a number of practical applications concerning several key industrial sectors including pharmaceutical, cosmetics, food processing, petroleum and bio-technology. In basic physical terms, the emulsification process consists of deforming successively an interface between two non-miscible fluids until fractionation of one of the

fluids in the form of small drops suspended in the other fluid is achieved. In isothermal conditions, the entropy increase associated to this fractionation process can solely be realized by supplying work in the form of a flow. Flows able to efficiently generate emulsions generally alternate in either an Eulerian or a Lagrangian frame of reference shear and extension. Examples of such flows are the laminar chaotic advection, [1, 2] or inertially turbulent flows, [3]. Of particular practical interest is the turbulent emulsification in open channel flows which allows continuous production of emulsions at high throughput. A kinematically favorable flow configuration that allows high throughput emulsification in a turbulent flow regime is the impinging jet configuration, [4]. Within this flow configuration, two non-miscible fluid streams undergo a head to head collision at large speeds (Reynolds numbers) which leads to a dramatic fractionation of the fluid interface(s) and ultimately results into an efficient emulsification. The first works that used impacting jets in order to achieve a liquid-liquid dispersion of non-miscible fluids date back to mid eighties, [5, 6]. More recently, the impinging jet configuration has been used with miscible fluids in micro-channels, [7], and for microscopic scale emulsification of Newtonian fluids, [4]. Impinging jets can generate small drops with narrowly distributed sizes at high throughput and the mean drop size is mainly affected by the relative speed of impact of the two fluid streams, [8].

Belkadi and coworkers investigated the process of water in a lipid phase emulsification that may be used as biofuel, [9]. They used an impinging flow microscopic flow system and found an optimal geometric configuration able to produce fine emulsions at high throughput while minimizing the energetic costs, [10].

Following this work, Ji et al. used the impinging flow device to generate oil-in-water (o/w) emulsions in a broad range of flow rates, [11]. They conclude that the more turbulent the microscopic flow is, the finer and more mono-dispersed the droplets will be.

With few exceptions including Refs. [12], [13], [14], [15] and [16], previous studies have been mainly restricted to Newtonian fluids while studying the liquid-liquid dispersion problem. As compared to the widely studied problem of Newtonian liquids dispersion in turbulent flows, the non-Newtonian rheological response of one of the two liquid phases brings a supplementary layer of complexity originating from the nonlinear relationship between the shear stresses and the rates of deformations to the hydrodynamic problem.

The previous studies of the liquid-liquid dispersion and emulsification focused on either viscoelastic [12, 17, 14, 18, 15] or shear thinning fluids [19, 20] as a continuous phase.

Shimizu and coworkers have measured the drop size distributions in stirred tanks with Newtonian and shear thinning fluids (aqueous solutions of carboxymethyl cellulose and xanthan gum), [21]. They show that the shear thinning behavior of the non-Newtonian continuous phase cause an increase in the maximum drop size and broadens the drop size distributions. The presence of xanthan gum in oil-in-water emulsions with Tween® 80 is generally believed to enhance the stability of the emulsions.

Also, by varying the xanthan concentration one can adjust the rheological and dispersion characteristics of the final emulsion [19].

Gu and coworkers have used xanthan solutions with various concentrations as dispersed phase and various oils used as continuous phase to study the formation time for drops in a T-junction, [20]. They observed that the droplet formation time decreased with increasing continuous and/or dispersed flow rates. Solutions with higher xanthan gum concentrations resulted in a longer formation time of the drops.

Chiarello and coworkers compared the formation of oil drops in Newtonian (aqueous solutions of glycerol) and non-Newtonian fluids (aqueous solutions of xanthan) in a T-junction microfluidic device, [16]. They found that xanthan solutions do not seem to significantly change the break-up process observed with aqueous solutions of glycerol.

The majority of the previous studies involving two-phase flows in the presence of non-Newtonian rheology focus on a laminar flow regime. As we are interested in high throughput emulsification in micro-channels, the relevance of these previous studies to the present work is somewhat limited. During turbulent flows of either viscoelastic or shear thinning solutions one typically observes the so called drag reduction phenomenon discovered over seven decades ago by Toms, [22]. To our best knowledge, the coupling between the drag reduction phenomenon and the generation of emulsions in the presence of shear thinning rheology at high throughput has not been investigated previously which sets the main scope of the present contribution. A first step towards understanding the physically complex problem of turbulent emulsification of shear thinning fluids has been undertaken in a recent study where the dynamics of a single drop in the turbulent impingement flow a xanthan solutions with various concentrations, [23]. This recent experimental study has shown that in the presence of a shear thinning rheological behavior of the continuous phase the dynamic modes of deformation and the breakup process of a single oil drop are profoundly altered.

Through the present study we investigate the influence of xanthan addition to the continuous phase on the dynamics of emulsification in a turbulent impingement flow in a micro-channel. Several fundamental aspects

are addressed herein. First, we assess the impact of shear thinning rheological behavior of the continuous phase on the granulometry of the final emulsion. Second, we discuss the flow regimes in a wide range of Reynolds numbers with a particular emphasis on the emergence of the drag reduction phenomenon. Third, we provide a systematic characterization of the liquid-liquid dispersion modes in connection to the rheological properties of the continuous phase. Last, we provide a space and time resolved characterization of the flow fields and discuss the results in the context of the drag reduction.

2. Methods

2.1. Microfluidic device

The experiments reported herein have been conducted in a cross-slot micro-channel schematically illustrated in Fig. 1. The micro-channel was machined from a single acrylic block with the dimensions 70 $mm \times 40$ $mm \times 18mm$ using a fast spinning (14000 rot/min) micro-milling head (Nakanishi, model $HES510 - BT40$) mounted on a commercial computer controlled milling machine (Twinhorn, model $VH1010$). The micro-milling technique has been previously used in microfluidics, [4, 24].

During the milling process, the depths of the micro-channel was accurately controlled over its entire length with an end to end variation smaller than one percent. The average roughness of the edges of the micro-channel as resulted from the micro-milling process is roughly of the order of a micron which accounts for less than a percent of the channel width. Unlike the more popular $PDMS$ micro-channels, the micro-milled micro-channels are able to sustain very large pressure drops (up to 90 $bars$) which is essential for performing experiments in a turbulent flow regime. The channel is closed by a second acrylic block fitted with o-rings to prevent fluid leakage via a set of stainless steel bolts, Fig. 1(a).

A critical requirement during our experiments was related to the large values of the operating pressures. To prevent fluid leakage during the experiments, both acrylic slabs had been sandwiched in between two aluminum made frames and armored with four stainless steel bolts.

The geometry of the micro-channel is detailed in Fig. 1(b). This cross-slot geometry has been proposed and studied by A. Belkadi and his coworkers for the case of Newtonian fluids, [9]. To produce water in oil emulsions oil is fed through an inlet with a squared cross-section $H_1 = W_1 = 300$ μm at a mass flow rate $\dot{m}_{i1}$ while a stream of xanthan solution is fed through an opposite inlet with dimensions twice larger $H_2 = W_2 = 600$ μm at a mass

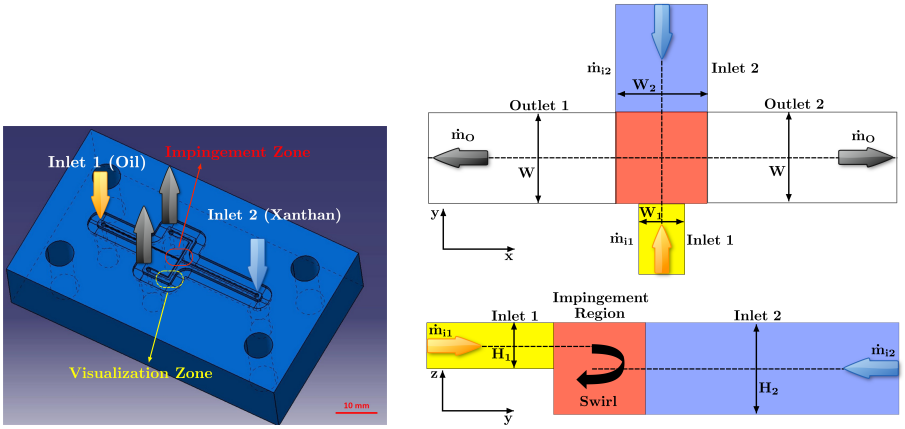

(a) (b)

Figure 1: (a) Schematic view of the microfluidic chip. The full line ellipse highlights the impingement zone while the dashed line ellipse the flow visualization zone. (b) **Top**: Frontal (camera) view of the cross-slot region in the (x, y) plane. **Bottom:** Lateral view (not accessible through our measurements but only hinted as) of the cross-slot region in the (y, z) plane. The colors are: blue and yellow regions refer to the channel inlets while the red highlighted region is the impingement zone. The *"cartoon"* arrow is solely a visual hint for the three dimensional flow structure dominated by the presence of a swirl located at the centre of the cross-slot region later referred to in the paper. In both panels the origin of the system of coordinates is located at the centre of the impingement zone.

flow rate $\dot{m}_{i2}$, top panel of Fig. 1(b). The uneven dimensions of the two fluid inlets have been purposely chosen in order to generate a swirling flow motion at the impact between the two fluid streams depicted in the cartoon illustrated in the bottom panel of Fig. 1(b). This swirling motion promotes the transition to turbulent flow states which plays a crucial role during the emulsification process.

After impacting within the impingement region highlighted by the red squares shown in Fig. 1(b) the fluids are discharged through two identical outlets. Both outlet channels have a squared cross section, $H = W = 600\ \mu m$. The flow rates of the discharged fluids are found to be equal (within 1%). The mean velocity at the outlets U_O is obtained by measuring the outlet mass discharge rates $\dot{m}_{o1} = \dot{m}_{o2} = \dot{m}_o$, [9, 25].

2.2. Ex-situ granulometry measurements

The granulometry of emulsion samples collected from the outlet fluid container is studied under a digital microscope ($KEYENCE\ VHX-7000$). The high-resolution images taken under the microscope are then analyzed manually using the ImageJ software. Based on the convergence of the average mean diameter towards a stable value, the sufficient number of measured droplets is determined in order to ensure the statistical relevance of the granulometry measurements.

The emulsification quality is quantitatively assessed mainly by evaluating the arithmetic mean diameter d_{10}. The active surface between the two phases in the emulsion relates to the potential interfacial energy stored. Therefore it is important to study the Sauter mean diameter d_{32}. The statistical convergence of the diameter measurements is monitoring the dependence of the mean diameter, the Sauter diameter and the uncertainty e of the droplet size on the number of drops accounted in the analysis. Through the reminder of the analysis, only statistically converged results are considered.

2.3. Experimental test bench

The flow control and data acquisition system are schematically illustrated in Fig. 2. The two fluids injected through the inlets of the micro-channel are held in the fluid containers $\mathbf{IFC_{1,2}}$. The two inlet fluid containers are mounted on two identical digital balances $\mathbf{DB_{1,2}}$ (Sartorius-MSE 2203) with an accuracy of 0.001 g which, connected to a personal computer $\mathbf{PC_1}$, provide a real time measurements of the flow rates $\dot{m}_{i1,i2}$. The sampling rate for the mass flow rate acquisition is 1 Hz. The inlet fluids are pumped into the micro-channel chip **MFC** by two pumps $\mathbf{P_{1,2}}$ ($AP\ TRIX$ 500 from Gilson, France). The fluids discharged through the two outlets of the micro-channel

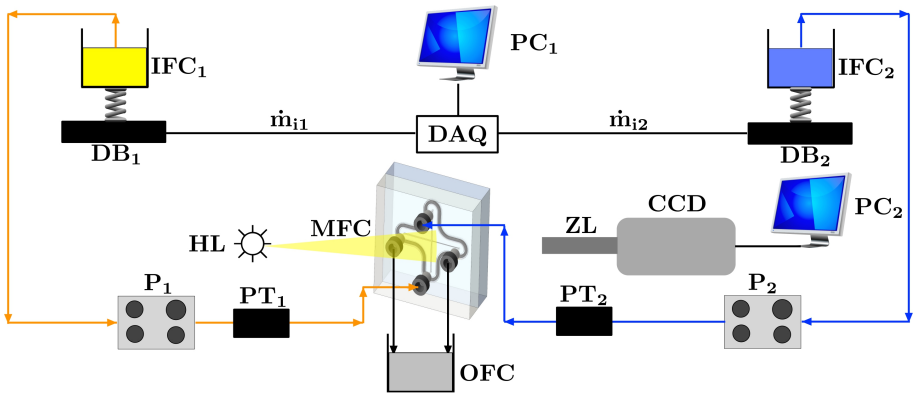

Figure 2: Schematic representation of the experimental system for the visualization of single drop dynamics: $\mathbf{IFC_{1,2}}$ - input fluid containers, **OFC** - output fluid container, $\mathbf{DB_{1,2}}$ - digital balances, $\mathbf{P_{1,2}}$ - fluid pumps, $\mathbf{PT_{1,2}}$ - pressure transducers, $\mathbf{PC_{1,2}}$ - data acquisition computers, **MFC**- microfluidic chip, **HL** - halogen lamp, **CCD** - digital camera, **ZL** - zoom lens.

in an outlet fluid container **OFC**. The micro-channel is illuminated from behind by a 50 W halogen lamp **HL** with its optical axis normally aligned to the centre of the impingement region of the micro-channel. The flow patterns are visualised by a fast camera **CCD** ($FASTCAME\ SA-X2\ 1080K\ M_4$ from Photron) equipped with a 12× magnification zoom lens **ZL** (Lavision) and connected to a second personal computer $\mathbf{PC_2}$.

The fast camera is equipped with an image intensifier and can be operated up to the nominal frame rate of 1080 $kfps$. The frame rate has been adjusted accordingly to the mean flow rates explored but never exceeded 540 $kfps$. To maximize the signal to noise ratio of the images, a maximum exposure time of $1/120000$ s has been set. The size of the acquired images (horizontal versus vertical) is 960 pixels by 320 pixels.

Two distinct flow visualisation strategies are used. For the characterization of the dispersion modes via direct visualisation of the fluid's interface, the micro-channel is illuminated from behind by a powerful white light source. For these experiments, no tracers or fluorescent dyes have been added and the position of the interface was identified by a different brightness induced by the difference in the refractive index of the two phase.

For the measurements of the flow fields, the micro-channel is illuminated laterally by a thin ($\approx 30\mu m$ at the beam-waist) laser sheet generated by a $10W$ solid-state laser in conjunction with a bespoke cylindrical optics system.

Both fluid streams (the oil and the aqueous solution of xanthan) have been seeded with hollow glass spheres with a diameter of $10\mu m$. The concentration of seeding particles has been adjusted iteratively in order to maintain a sufficient number of tracers in the filed of view.

To obtain time series of flow fields, the flow images have analyzed by an open source Particle Image Velocimetry software package implemented under Python, [26]. Thus, time series of velocity separated in time by 0.01 ms were acquired for various values of the driving flow rates.

2.4. Choice and physical characterization of the fluids

2.4.1. Choice of the fluids

As a continuous phase we have used aqueous solutions of xanthan gum. The xanthan gum is a biopolymer produced by a soil bacterium *Xanthomonas campestris* and is one of the most popular hydrocolloids used in various industrial sectors (cosmetics, pharmaceuticals, energy, enhanced oil recovery) applications. This gum is an anionic hetero-polysaccharide consisting of a linear cellulose skeleton of β-D-glucoses of which every second unit is substituted in C_3 by a trisaccharide side chain. Xanthan gum solutions are known to present a significant shear thinning behavior that becomes more pronounced as the polymer concentration is gradually increased [27]. More specifically, several concentration regimes can be encountered according to the polysaccharide concentration used, [28]. The *"dilute regime"* is characterized by small or no steric effects which translates into a weakly shear-thinning behaviour, [29]. Beyond a critical concentration, denoted as C^*, physical interaction gets significant between molecules, [30]. The corresponding regime is coined as the *"semi dilute regime"*. However, internal forces are still dominated by the interactions between the solvent and the polymer [31]. A second critical concentration value, C^{**}, defines a limit beyond which the system is in the *"concentrated regime"* in the sense that the polymer molecules become entangled. Above the overlap concentration the viscosity increases significantly with the polymer concentration, and a pronounced shear-thinning behavior is observed [29].

The experiments reported herein were performed with a commercial xanthan gum purchased in an anhydrous form ($Kelzan\ T$ from CP Kelco) and dissolved in tap water containing 0.5% ($wt.$) of Tween® 20 as a surface agent added to the solvent. This concentration is well above the critical micellar concentration ($CMC \approx 0.0074\%\ (wt)$) and low enough in order not to alter the properties of the solution. The xanthan solutions used through this study were formulated at nine different concentrations ($0.05\%(wt.)$, $0.075\%(wt.)$, $0.09\%(wt.)$, $0.1\%(wt.)$, $0.15\%(wt.)$, $0.2\%(wt.)$, $0.3\%(wt.)$, $0.4\%(wt.)$ and

$0.5\%(wt.)$). It is difficult to find universal values for bounds of the three concentration regimes C^* and C^{**} based on the literature survey described above. This is mainly due to the physico-chemical variety of xanthan gums used by various authors and to the various methodologies applied. We have used as a dispersed phase commercially available sun flower oil (from Carrefour, France) with a density 865 kg/m^3 a viscosity of 52.5 $mPas$ and a surface tension of 33.7 mN/m at room temperature.

2.4.2. Interfacial properties of the fluids

The interfacial tension σ_i for the different xanthan gum solutions with oil was measured using a $KRUSS$ $K12$ tensiometer with the plate method according to Wilhelmy at $T = 25^oC$.

For each solution, the interfacial tension with oil was measured three different times in order to test the repeatibility. The presence of xanthan gum in the solution did not affect the interfacial tension with oil as the values of this latter for the different concentrations of xanthan were similar to that for water (with $0.5\%(wt.)$ of Tween® 20 as a surfactant). Thus, the interfacial tension with oil for all solutions is chosen to be that of water with 0.5% $(wt.)$ of Tween 20 which is $\sigma_i \approx 5.4$ mN/m at $T = 25^oC$.

2.4.3. Rheological characterization of the fluids

It was important to characterize the rheological behavior of the xanthan solutions used in this study in a broad range of shear rates relevant to the experiments herein, performed at high flow rates in an inertially turbulent regime. Therefore, two techniques were combined: conventional rotational rheometry and high shear rate microfluidic rheometry [32].

The classical rotational rheometry tests were performed using a Mars-III (Thermofischer Scientific) device which is a controlled stress rotational rheometer equipped with a nano-torque module. Tests were performed using a cone and plate geometry with a radius $R = 30$ mm and a truncation angle $\alpha = 2°$ ($C60/2°$ TiL for HAAKE MARS). The temperature was regulated at $25 \pm 0.05°C$ using both a Peltier system embedded in the bottom plate of the rheometer and an electrical oven enclosure mounted on the top of the geometry. The number of steps for each branch of the ramp was $N = 100$ and the averaging time per step was 30 s. Measurements have been performed by imposing increasing/decreasing controlled shear rate ramps ranging from 1 s^{-1} to a maximal shear rate $\dot{\gamma}_c$ beyond which inertial instabilities are expected to occur within the cone-plate flow. Each rheological measurement was repeated a second time with a new sample of each solution to test the repeatability.

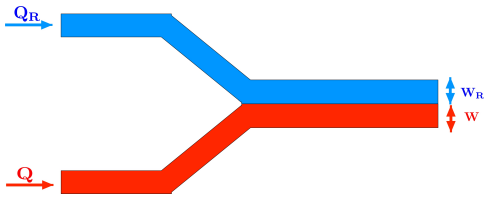

Figure 3: Schematic representation of the high shear rate microfluidic rheometer: Q - flow rate of the fluid to be characterized, Q_R - flow rate of the reference fluid with a known viscosity, W - transversal extent of the fluid to be characterized, W_R - transversal extent of the fluid reference fluid.

The high shear rate rheological tests have been performed using a microfluidic rheometer (FLUIDICAM RHEO^{TM} from Formulaction, France) which allows one to probe a broad range of shear rates depending on the fluid properties, $\dot{\gamma} \in \left[100\ s^{-1}, 2 \cdot 10^5\ s^{-1}\right]$. A detailed description of the operating principle of this device can be found in [33]. The fluid to be characterized is injected side by side with a reference fluid (with a known viscosity) in Y shaped micro-channel [34] with a width $W_{total} = W + W_R = 2200\ \mu m$ as schematically illustrated in Fig. 3. Using successively two microchips with channels of different heights, $h = 50\ and\ 150\ \mu m$ allows to cover the above cited shear rates range.

The flow rates Q_R and Q of the reference fluid and of the fluid to be characterized are precisely controlled using two accurate micro-syringe pumps. As a reference Newtonian fluid, an aqueous base solution was used with a viscosity of $\eta_R = 6\ mPa \cdot s$ at $T = 25^oC$.

Due to the small size of the channel the flows are laminar and fully developed at the channel outlet. The actual position of the interface occupied by the fluids is measured by acquiring a time series of images of the interface between the two fluids. The ratio of the transverse extents of the two fluids W/W_R near the outlet of the microfluidic device is determined by subsequent image processing. It is proportional to the ratio of the apparent viscosity η_{app} of the fluid to be characterized and the known viscosity η_R of the reference fluid, [35, 36]:

$$\frac{W}{W_R} = \frac{\eta_{app}}{\eta_R} \frac{Q}{Q_R} \tag{1}$$

Thus, according to the simple relationship above, monitoring optically the ratio $\frac{W}{W_R}$ and knowing the flow rates Q and Q_R allows one to extract the ratio $\frac{\eta_{app}}{\eta_R}$ between the apparent viscosity of the fluid to be characterized to

the known viscosity of the reference fluid.

The true rate of shear experienced by the fluid to be characterized may be expressed according to Weissenberg-Rabinowitsch-Mooney equation, [37]:

$$\dot{\gamma}_{true} = \frac{\dot{\gamma}_{app}}{3}\left[2 + \frac{d\ \ln \dot{\gamma}_{app}}{d\ \ln \tau}\right] \tag{2}$$

Here $\dot{\gamma}_{app} = \frac{6Q}{Wh}$ stands for the apparent rate of shear and $\tau = \dot{\gamma}_{true}\eta = \dot{\gamma}_{app}\eta_{app}$ is the true stress imposed onto the tested fluid,[38].

2.5. Rheological behavior of the xanthan solutions at various concentrations

Aqueous solutions of xanthan gum are generally known to present a significant shear thinning behavior that becomes more pronounced as the polymer concentration is gradually increased [27].

To get a full picture of the various rheological regimes observed when the xanthan concentration is varied in a wide range relevant to our emulsification experiments, systematic measurements of the steady state viscosity are performed by combining rotational and microfluidic rheometry, Fig. 4. The full symbols correspond to measurements performed via classical rotational rheometry while the open symbols refer to high shear rate microfluidic measurements.

The better assess the zero shear viscosity controlled stress measurements have been equally performed, 4(b). As widely acknowledged in the literature, regardless the value of the xanthan concentration, a shear thinning behavior is observed. This is typically described by the Carreau-Yasuda model (the full lines in panel 4(a)):

$$\eta = \eta_\infty + (\eta_0 - \eta_\infty)\left[1 + (\lambda\dot{\gamma})^2\right]^{(n-1)/2} \tag{3}$$

Here $\eta_0 = \lim_{\dot{\gamma}\to 0}\eta\left(\dot{\gamma}\right)$ stands for the zero shear viscosity, $\eta_\infty = \lim_{\dot{\gamma}\to\infty}\eta\left(\dot{\gamma}\right)$ for the infinite shear viscosity, λ sets a scale $(1/\lambda)$ for the shear rate marking the onset of the shear thinning behavior and $n \in [0, 1]$ is the power law index that characterizes the steepness of the shear thinning behavior observed between the two viscosity plateaus.

The non-linear fitting parameters for the different xanthan gum solutions are presented in Table 1. Additionally, Table 1 shows the values of the mean absolute percentage error $MAPE$ (%) between the rheological data and the model such that:

$$MAPE = \frac{100\%}{j}\sum_{i=1}^{j}\left|\frac{\eta_i - \eta_{CY,i}}{\eta_i}\right| \tag{4}$$

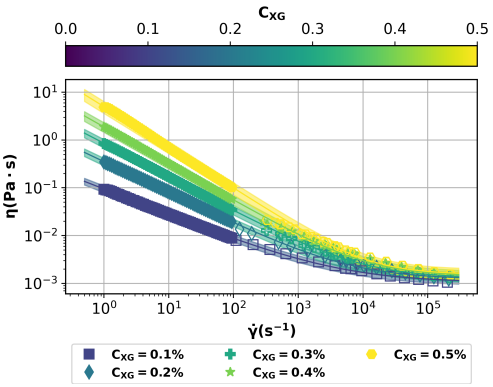

(a)

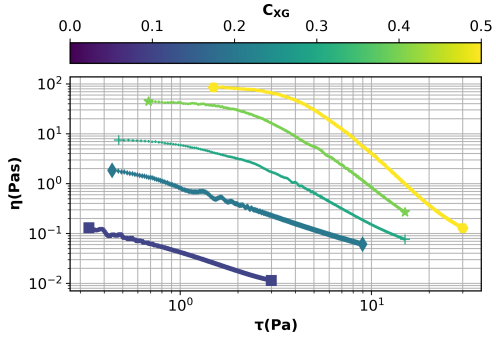

(b)

Figure 4: Steady state rheological measurements performed at controlled rate of deformation (panel (a)) and at controlled stress (panel (b)). The full lines in panel (a) are nonlinear fitting functions obtained according to the Carreau-Yasuda model. In each panel the highlighted regions indicate the instrumental error. The full symbols refer to the classical rotational rheometric measurements while the open symbols to the microfluidic ones.

Solution	η_0 $(mPa.s)$	η_∞ $(mPa.s)$	λ (s)	n	$MAPE$ (%)
$C_{XG} = 0.1\%$	623	1.05	33.6	0.46	1.76
$C_{XG} = 0.2\%$	2170	1.23	16.4	0.35	3.2
$C_{XG} = 0.3\%$	4260	1.48	12.1	0.33	8.86
$C_{XG} = 0.4\%$	23320	1.6	5.76	0.22	4.03
$C_{XG} = 0.5\%$	44100	1.66	3	0.12	6.96

Table 1: Fitting parameters for the different xanthan gum solutions following the Carreau-Yasuda model.

where η_i and $\eta_{CY,i}$ are the viscosity values obtained from the rheological measurements and using the non-linear fitting parameters respectively.

A quick comparative inspection of the viscosity data plotted versus the stress (panel 4(b)) reveals an important qualitative detail. For xanthan concentrations $C_{XG} \geq 0.3$ a clear low stress viscosity plateau develops. This together with the rather large values of the zero shear viscosity has prompted us to question if the rheological behavior is a classical Carreau-Yasuda one or some mild yield stress behavior comes into play. To test this hypothesis, we have performed creep tests by imposing a constant stress and monitoring the long time asymptotic behavior of the strain. When a material is subjected to a constant stress the strain scales with time as a power law $\gamma \propto t^\alpha$ in the asymptotic limit of long times. A constant and finite viscosity regime corresponds to $\alpha = 1$. When $\alpha < 1$ a viscoplastic deformation regime is observed. Indeed, if $\alpha < 1$ then the rate of shear $\dot{\gamma} \propto t^{\alpha-1}$ is a monotonically decreasing function of time $lim_{t\to\infty}\dot{\gamma} = 0$ and the flow stops in a finite time. Bearing in mind these simple considerations, to distinguish the viscous flow deformation regime from the yield stress regime it is sufficient to measure the scaling exponent α for several values of the imposed stress.

We exemplify measurements performed during creep tests performed for various values of the imposed stress τ_0 in Fig. 5. For $C_{XG} = 0.2\%$ a linear asymptotic scaling of the strain is observed indicated a viscous behavior, panel 5(a). A substantially different behavior is observed for a highly concentrated xanthan solution. For low values of the applied stress, the scaling exponent of the strain appears to be smaller than unity. This leads to flow stoppage in a finite time and is a signature of viscoplastic rheological behavior, [39].

The question of existence of yield stress has been rarely studied. Recently, Ong and coworkers suggested that solutions of XG at high concentrations (0.4% to 1%) in deionized water could exhibit yield stress, [40]. They also indicated through their study that, within this range of concentrations, the

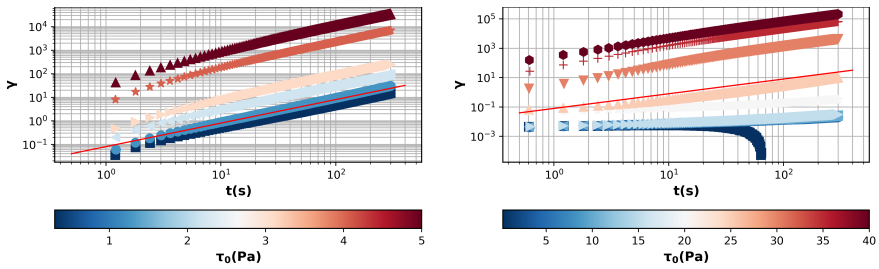

Figure 5: Time dependence of the strain obtained via creep tests performed for various stresses τ_0 and two xanthan concentrations: (a) $C_{XG} = 0.2\%$ (b) $C_{XG} = 1\%$. In both panels the data sets are color indexed by the value of the imposed stress τ_0 (see the bottom color-bars). The full line is a guide for the eye, $\gamma \propto t^1$.

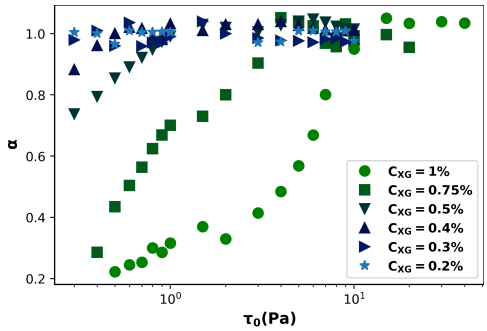

Figure 6: Dependence of the scaling exponent α on the stress σ_0 imposed during the creep tests. The symbols are detailed in the figure insert.

xanthan solutions exhibit a thixotropic behaviour.

In order to map the viscoplastic behavior, we have performed creep tests similar to the ones illustrated in Fig. 5 and obtained the values of the scaling exponents α. This result is presented in Fig. 6. For xanthan solutions with concentrations $C_{XG} \leq 0.2\%$ a roughly unitary scaling exponent is found of order of unity over the entire range of applied stresses (the stars and the right triangles in Fig. 6). For larger concentrations, $C_{XG} \geq 0.3\%$, we systematically identify a critical stress value τ_y beyond which the scaling exponents switches from a unitary value to a sub-unitary one. Based on this result, we may conclude that, within this range of concentrations, the xanthan solutions clearly exhibit a viscoplastic rheological behavior.

Additional evidence of an apparent yield stress behavior, revealed via

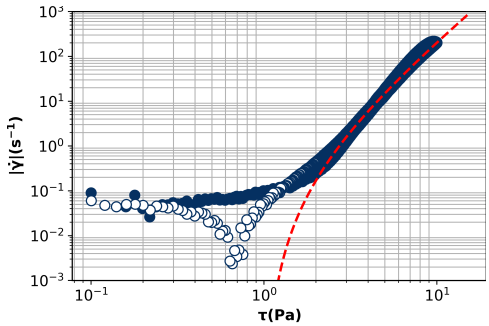

Figure 7: Measurements of the absolute value of the rate of deformation $|\dot{\gamma}|$ performed during a controlled increasing (full symbols) and decreasing (empty symbols) stress ramps with a $C_{XG} = 0.5\%$ xanthan solution.

the creep tests for $C_{XG} \geq 0.3\%$, may be obtained by performing increasing/decreasing controlled stress ramps. We illustrate in Fig. 7 such measurements performed with a $C_{XG} = 0.5\%$ xanthan solution during a linear stress ramp. On both the increasing (full symbols) and decreasing (empty symbols) branch of the stress ramp, for stresses $\tau \leq \tau_y$ ($\tau_y \approx 1Pa$), the measured shear rates exhibit a plateau. Bearing in mind that the stresses vary linearly with time, this is consistent with an elastic solid behavior described by Hooke's law. Beyond this onset a fluid behavior described by the Herschel-Bulkley law is observed (the dashed line in Fig. 7). These measurements are an alternative proof for the yield stress behavior of the xanthan solutions in this range of concentrations.

As opposed to the Carreau-Yasuda rheological behavior which is well documented in previous studies, the yield stress behavior of xanthan solutions has received much less attention. A full account of the yielding behavior of concentrated xanthan solutions will be provided in a subsequent publication.

To fully map the rheological regimes discussed above, we plot the dependence of the zero shear viscosity on the xanthan concentration, Fig. 8. Although the ionic content of our solutions was not controlled (due to the usage of tap water), these measurements are in a rather good agreement with previous measurements reported in Ref. [41] (see Fig. 8 therein) and four distinct scaling regimes may be observed.

For $C_{XG} \leq C^*$ ($C^* \approx 0.055\%$) a dilute regime is observed. The *"dilute regime"* is characterized by small or no steric effects which translates into a weakly shear-thinning behaviour, [29]. Within the dilute regime the zero shear viscosity scales with the xanthan concentration as $\eta_0 \propto C_{XG}^{1.28\pm0.12}$.

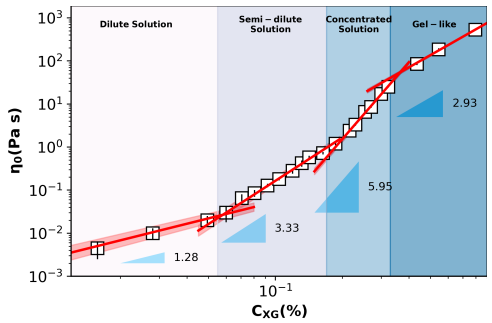

Figure 8: Dependence of the zero shear viscosity η_0 on the concentration of xanthan C_{XG}. The four distinct shaded areas mark the various concentration regimes. The vertical arrows point the concentration bounds that delineate the four regimes: C^*, C^{**}, C^e (see text for discussion). The lines are power law fitting functions and the shadded area overlap onto them highlight the fit error (see text for details/discussion).

A semi-dilute regime is observed for $C_{XG} \in [C^*, C^{**}]$ where $C^{**} \approx 0.16\%$. Within this regime the physical interactions between molecules becomes significant, [30]. Consequently, within the semi-dilute regime the zero shear viscosity scales with the xanthan concentration as $\eta_0 \propto C_{XG}^{3.33\pm0.18}$.A concentrated regime is observed for $C_{XG} \in [C^{**}, C^e]$ where $C^e \approx 0.33\%$ and, within this regime, the zero shear viscosity scales as $\eta_0 \propto C_{XG}^{5.95\pm0.13}$. This regime is characterized by a very pronounced shear-thinning behavior [29]. Upon a farther increase of the concentration $C_{XG} \geq C^e$ a fourth scaling regime is observed, $\eta_0 \propto C_{XG}^{2.93\pm0.15}$.

To our best knowledge, data on the scaling of the zero shear viscosity with the xanthan concentration are rather scarce in the literature. We compare in the following our scaling results with those obtained by Nsengiyumvaa and Alexandridisa. [42]. As a polymer, they have used a similar one. The scaling behavior they found within the semi-dilute regime is very different than ours ($\eta_0 \propto C_{XG}^{0.5}$ while we found $\eta_0 \propto C_{XG}^{3.33}$). The scaling behaviour they found in the concentrated regime is also quite different ($\eta_0 \propto C_{XG}^{1.5}$ while we found $\eta_0 \propto C_{XG}^{5.95}$). We attribute these significant discrepancies to several factors: possible differences in the grade of xanthan, differences in the salt content of the solutions (as previously stated, our solutions were prepared in tap water so their ionic content was not controlled) and possible differences in the rheometric procedure. A better agreement of the scaling behavior illustrated in Fig. 8 is found with measurements presented Ref. [41] for xanthan solutions containing $50mM\ NaCl$ (see Fig. 8 therein) who found $\eta_0 \propto C_{XG}^{1}$ in the dilute regime, $\eta_0 \propto C_{XG}^{2}$ in the semi-dilute regime

and $\eta_0 \propto C_{XG}^{4.67}$ in the concentrated regime.

3. Results

Prior to detailing the main experimental findings, we discuss in the following the relevant non-dimensional groups characterizing the emulsification process.

To characterize the hydrodynamic state of the flow and monitor the laminar-turbulent transition, the bulk Reynolds number is defined as $Re_{i2} = \frac{\rho U_{i2} H_2}{\eta}$. The viscosity η used in this definition is obtained from the rheological measurements via interpolation at the characteristic rate of shear estimated via the pressure drop, $\dot{\gamma}_{i2} = \frac{2Q_{i2}}{H_2 W_2^2}$. Within the microchannel, the rates of shear can reach $10^5\ s^{-1}$.

By varying the flow rates and the xanthan concentration (the kinematic viscosity), the bulk Reynolds number has been varied in the range $Re_{i2} \in [300, 16000]$. As it will be shown later in Sec. 3.2, this range of Reynolds numbers covers laminar, transitional and fully developed turbulent flow states.

The relative importance of inertial and capillary effects is quantified by the Weber number, $We_d = \frac{\rho Ui2^2 d_{10}}{\gamma_{w/o}}$. By varying the flow rates, the xanthan concentration in the continuous phase and accounting for the ex-situ measurements of the mean drop diameter, the Weber number was varied through our experiments in the range $We \in [32, 506]$.

The balance between viscous effects and combined inertia and capillarity is quantified by the Ohnesorge number, $Oh_d = \frac{\eta}{\sqrt{\rho \gamma_{w/o} d_{10}}}$, which was varied through the granulometry experiments in the range $Oh_d \in [1.12, 68] \times 10^5$. It is instructive to estimate the time scales relevant to the emulsification experiments described in this work. A first relevant time scale is the residence time of the fluid interfaces within the emulsification micro-channel which ranges in between 1.6 ms and 7.9 ms. In the presence of inertia, capillarity and viscous effects there exist three intrinsic time scales relevant to the turbulent emulsification process. The inertio-capillary time scale is defined as $\tau_{ic} = \sqrt{\frac{\rho d_{10}^3}{\gamma_{w/o}}}$ and it was varied through our experiments in the range $\tau_{ic} \in [2\ ms, 60\ ms]$. The viscous-inertial time scale defined as $\tau_{vi} = \frac{\rho d_{10}^2}{\eta^2}$ was varied in the range $\tau_{vi} \in [10\ ms, 290\ ms]$. Finally, the Ohnesorge time scale is defined by $\tau_O = \frac{\eta^3}{\rho \gamma_{w/o}^2}$ and it was varied in the range

$\mathbf{C_{XG}}$ (%wt.)	$\mathbf{Q_{i2}}$ ($\times\mathbf{10^2}$ mL/min)	$\mathbf{d_{10}}$ (μm)	$\mathbf{Re_{i2}}$ ($\times\mathbf{10^3}$)	$\mathbf{We_d}$	$\mathbf{Oh_d}$ ($\times\mathbf{10^4}$)	$\tau_{\mathbf{vi}}$ (ms)	$\tau_{\mathbf{O}}$ (ns)	$\tau_{\mathbf{ic}}$ (ms)
0	[1, 5]	[3, 8]	[3, 15]	[30, 270]	[52, 407]	[10, 70]	31.6	[2, 9]
0.05	[1, 5]	[4, 12]	[2, 13]	[45, 386]	[30, 244]	[10, 130]	[37, 42]	[3, 19]
0.075	[1, 5]	[4, 14]	[2, 11.5]	[57, 364]	[24, 275]	[10, 150]	[40, 48]	[3, 23]
0.09	[1, 3]	[8, 16]	[1.9, 6.35]	[66, 271]	[20, 73]	[50, 170]	[45, 52]	[9, 28]
0.1	[1, 5]	[3.7, 16]	[1.8, 11]	[65, 379]	[21, 315]	[10, 160]	[44, 54]	[3, 27]
0.15	[1, 5]	[4, 15]	[1.58, 10]	[48, 59]	[21, 315]	[10, 130]	[12, 309]	[3, 26]
0.2	[1, 5]	[2.8, 14]	[1.5, 3]	[55, 250]	[35.8, 678]	[10, 100]	[51, 65]	[2, 22]
0.3	[1, 3]	[14, 22]	[1, 5]	[92, 506]	[14.7, 30]	[66, 230]	[60, 77]	[23, 47]
0.4	[1, 3]	[11, 27]	[1.1, 4]	[109, 388]	[12, 57]	[60, 290]	[66, 88]	[15, 60]

Table 2: Summary of the granulmometry experiments. C_{XG} stands for the xanthan concentration, Q_{i2} for the volumetric flow rate of the continuous phase, d_{10} for the arithmetic mean diameter, Re_{i2} for the bulk Reynolds number, We_d for the diameter Weber number, Oh_d for the diameter Ohnesorge number, t_{vi} for the viscous-inertial time scale, τ_O for the Ohnesorge time scale and t_{ic} for the inertio-capillary time scale.

$\tau_O \in [31.6\ ns, 88\ ns]$. For the emulsification experiments reported through the paper, $\tau_O < \tau_{ic} < \tau_{vi}$.

3.1. Ex-situ granulometry of the suspensions for various xanthan concentrations

To address how the shear thinning nature of the continuous phase influences the properties of the final emulsion, we focus through this section on an ex-situ characterization of the emulsions obtained in various flows conditions (essentially Reynolds numbers) for various concentrations of xanthan C_{XG} in the continuous phase.

The microfluidic experiments performed for the granulometry study are listed in Tab. 2.

The drop diameters are statistically distributed according to a log normal distribution (data not shown here) which has been previously observed for emulsions obtained in turbulent flows [43, 44].

Ex-situ measurements of the arithmetic diameter of the suspensions obtained for several distinct pairs of driving flow rates and for various concentrations of xanthan in the continuous phase are exemplified in Fig. 9.

For the pairs of the largest driving flow rates $400 - 21\ mL/min$ and $500 - 27\ mL/min$ (the diamonds and hexagons) the mean diameter does not depend on the xanthan concentration. Intuitively, this may be understood as follows. At such large driving flow rates the local rates of shear within

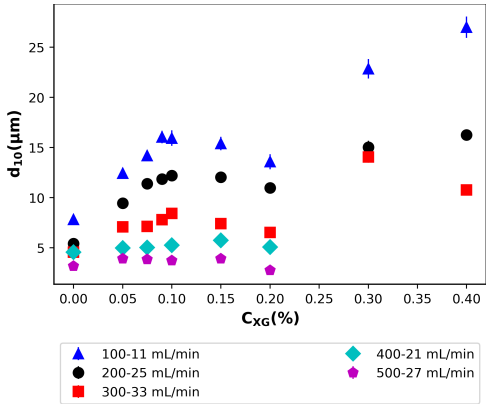

Figure 9: Variation of the emulsions' arithmetic mean diameter with the concentration of xanthan in the continuous phase for several flow rate couples Q_{i2}, Q_{i1}detailed in the lower insert.

the micro-channel are sufficiently large so the xanthan solutions roughly behave as Newtonian fluids. For the smaller flow rates exemplified in Fig. 9 the dependence of the mean diameter of the resulting emulsions on the xanthan concentration is clearly non-monotonic: a local maximum systematically develops around $C_{XG} \approx 0.1\%$ and a local minimum is apparent around $C_{XG} \approx 0.2\%$. It is rather clear that within this range of flow rates the non Newtonian rheological behaviour of the continuous phase plays an important role.

In closing the granulometry measurements of the obtained emulsions, let us relate these results summarized in Fig. 9 to the various rheological regimes mapped in Fig. 8. Around $C^* \approx 0.055\%$, we do not observe any particular change in the trend of the measured mean diameters. However, a local maximum of the mean diameters is observed around $C^{**} \approx 0.1\%$ for the first three flow rates investigated (the triangles, the circles and the squares in Fig. 9). Past the onset of the entangled regime $C_e \approx 0.3\%$ where the viscoplastic rheological behavior is observed, a dramatic change in the trend of the mean diameters is observed for the same first three flow rates illustrated in Fig. 9.

Based on the comparative discussion presented above, one may conclude that there exists a clear relationship between the ex-situ assessed granulometry of the emulsions and the rheological behavior of the continuous phase.

$\mathbf{C_{XG}}$ (%wt.)	$\mathbf{Q_{i2}}$ (mL/min)	$\mathbf{P_{i2}}$ (bar)	$\mathbf{Re_{i2}}$ ($\times 10^3$)	$\mathbf{Re_o}$ ($\times 10^3$)	Ca
0	[50, 500]	[0.52, 23.1]	[1.5, 15.6]	[0.82, 8.5]	[0.2, 2.2]
0.05	[50, 500]	[0.56, 21.9]	[1, 12.5]	[0.56, 6.8]	[0.3, 2.5]
0.075	[50, 500]	[0.62, 21.9]	[0.98, 12]	[0.53, 6.5]	[0.4, 2.8]
0.09	[50, 500]	[0.68, 22.2]	[0.79, 10.5]	[0.43, 5.8]	[0.4, 2.8]
0.1	[50, 500]	[0.84, 22.8]	[0.8, 11]	[0.43, 6]	[0.44, 3]
0.15	[50, 500]	[0.92, 24.5]	[0.65, 9.8]	[0.35, 5.3]	[0.49, 3.2]
0.2	[50, 500]	[1.14, 25.3]	[0.57, 9.3]	[0.31, 5]	[0.52, 3.4]
0.3	[50, 500]	[1.6, 25.1]	[0.5, 8.5]	[0.27, 4.6]	[0.67, 3.7]
0.4	[50, 500]	[1.9, 25.1]	[0.46, 8.3]	[0.25, 4.5]	[0.83, 4.3]
0.5	[50, 500]	[1.9, 30]	[0.31, 7.2]	[0.17, 4]	[1, 4.2]

Table 3: Summary of the experiments. C_{XG} stands for the xanthan concentration, Q_{i2} for the volumetric flow rate of the continuous phase, P_{i2} for the relative pressure of the continuous phase, Re_{i2} for the bulk Reynolds number of the continuous phase, Re_o for the bulk Reynolds number of the output flow and Ca for the capillary number.

3.2. Description of the flow regimes

As it is rather clear from Fig. 9 that the final granulometry of the emulsions is intrinsically related to the driving flow rates it is natural to provide a systematic characterization of the hydrodynamic flow regimes. To do so, we focus in the following on integral measurements of the pressure drops driving the flow and assess various flow regimes by monitoring their dependence on the Reynolds number Re_{i2}.

The experiments reported through this section are performed using various xanthan solutions with concentrations spanning a broad range ($C_{XG} \in [0\%, 0.5\%]$) as a continuous phase and within a range of driving flow rates relevant to the emulsification process. The details of the experiments and the values of the relevant non-dimensional quantities are listed in Tab. 3.

The ratio between the flow rate of the dispersed phase and the flow rate of the continuous phase was fixed. $\Phi_o = \frac{Q_{i1}}{Q_{i2}} = 10\%$. For each xanthan concentration a wide range of flow rate couples are tested with the flow rate of the continuous phase Q_{i2} ranging in between 50 mL/min and 500 mL/min.

The dependence of the driving pressures P_{i2} on the Reynolds numbers Re_{i2} measured for various xanthan concentrations in the continuous phase is shown in Figure. 10(a).

Regardless the concentration of xanthan in the continuous phase, the pressure depends linearly on the Reynolds number up to a critical value $Re_{i2}^c \approx 2300$- the dashed lines in Fig. 10(a). This corresponds to a laminar flow state. Beyond this critical Reynolds number, the pressure drops enter

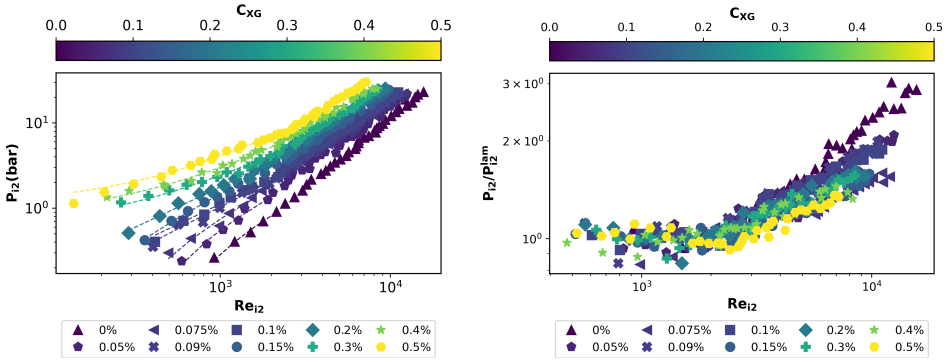

(a) (b)

Figure 10: (a) Dependence of the pressure drop on the Reynolds number measured for various concentrations of xanthan in the continuous phase. The dashed lines are linear fitting functions. (b) Normalized (by the laminar part) pressure drops versus Reynolds numbers for the various concentrations of xanthan in the continuous phase solution.

a power law scaling regime which is steeper than linear corresponding to turbulent flow states.

This increased slope of the pressure drop dependence observed in a turbulent flow regime is commonly termed as *"flow resistance"* and represents a quantitative measure of the energetic costs associated to the transition from laminar flow states to turbulent ones. To quantitatively assess the flow resistance associated to the transition to turbulence when xanthan solutions with various concentrations are used, we compute the reduced pressure drops $\bar{P}_x = \frac{P_{i2}}{P_{lam}}$, Fig. 10(b). Here P_{lam} is defined by the linear fit of the pressure data acquired within the laminar flow regime, $Re < Re_{i2}^c$ - see the dashed lines in Fig. 10(a).

The addition of xanthan leads to a decrease of the apparent flow resistance. We associate this observation with the emergence of the well known phenomenon of drag reduction previously observed with xanthan solutions, [45, 46]. This assertion is also based on the time series analysis presented in the further section 3.4.

For a quantitative assessment of the drag reduction effect, we define a reduced flow parameter:

$$RFR(\%) = \frac{\bar{P}_w - \bar{P}_x}{\bar{P}_w} \tag{5}$$

Here $\bar{P}_w$ is the normalized pressure for water and $\bar{P}_x$ is that for a xanthan gum solution.

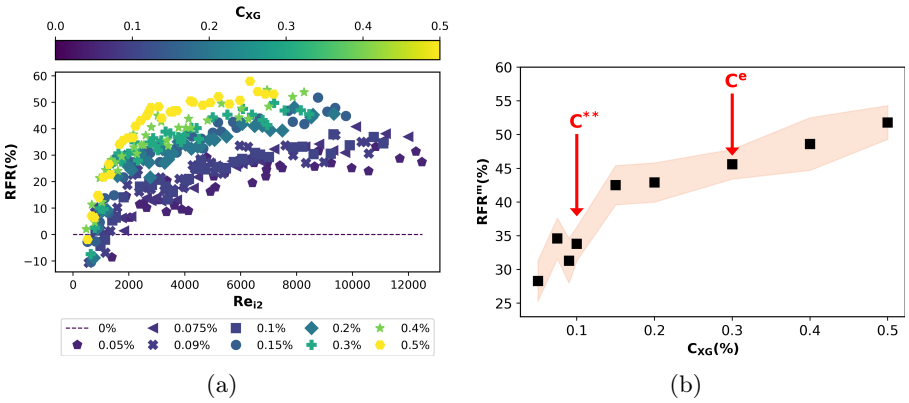

(a) (b)

Figure 11: (a)Variation of the reduced flow resistance with the Reynolds numbers and the different concentrations of xanthan in the continuous phase solution. (b) Dependence of the plateau value of the reduced flow resistance (RFR) on the xanthan concentration. The shaded region highlights the level of fluctuations of RFR around its plateau value.

We note that our approach of quantitatively assessing the drag reduction according to Eq. 5 is substantially different from that used in previous studies where a drag reduction coefficient DR is defined via the wall shear stress (see for example Ref. [47] and the references therein). This choice can be motivated in relation to the shape of the micro-channel which departs strongly from a simple pipe flow geometry previously used by others. The total flow resistance in the case of the micro-channel studied herein comes from seven distinct contributions which are not necessarily additive: the flow resistance in the oil inlet (obviously unaffected by the drag reduction), the flow resistance from the aqueous phase inlet (affected by drag reduction), two flow resistance components in the outlets of the channel (partially affected by the drag reduction), two flow resistances from the presence of the 90° edge and the widening section prior to the exit of the channel and the flow resistance due to the presence of the swirl induced by the uneven fluid inlets in the impingement zone. As in the case we study, these contributions depend on the Reynolds number and, to our best understanding, can not be easily decoupled so the classical definition of the drag reduction coefficient becomes unpractical.

The main results on the reduced flow resistance are summarized in Fig. 11. The dependence of the reduced flow resistance RFR on the Reynolds number calculated for various xanthan concentrations in the continuous phase is illustrated in Fig. 11(a).

For each xanthan concentration, past the onset of fully developed turbu-

lent flow $Re_{i2} \geq 2300$, the reduced flow resistance reaches a plateau.

The plateau values of the RFR increase with the xanthan concentration reaching nearly 50% for $C_{XG} = 0.5\%$, Fig. 11(b). Quite interestingly, the trend of this dependence changes twice in the points marked by vertical arrows which correspond to $C_{XG} = C^{**}$ and $C_{XG} = C^{e}$. This highlights the strong coupling between the various rheological regimes summarized in Fig. 8 and the turbulent flow regimes.

3.3. Dynamic regimes of the microscopic emulsification

The integral measurements of the pressure drop detailed in Sec. 3.2 highlight both the transition from laminar flow states to turbulent and the emergence of drag reduction when xanthan is added to the continuous phase but provide no information about the microscopic dynamic regimes of the interfaces during the emulsification process.

With Newtonian fluids, various liquid-liquid dispersion patterns are commonly observed in micro-channels: parallel flow, annular flow, slug flow, plug flow, deformed interface flow or droplet flow. These flow patterns are selected in relation to the geometry, size and wettability of the microchannel, the topology of the inlet junctions, the properties of the two liquids and the flow conditions [48, 49, 50, 51].

This section is dedicated to the characterization of these dynamic regimes with a particular focus on the correlation between these regimes and the rheological regimes discussed in Sec. 2.5 and summarized in Fig. 8.

To characterize the dynamics of the interfaces between the continuous and the dispersed phase, experiments have been performed using as a continuous phase distinct xanthan solutions with concentrations C_{XG} ranging from $0\%(wt.)$ (pure water) to $0.5\%(wt.)$. The ratio between the flow rate of the dispersed phase and the flow rate of the continuous phase was fixed. $\Phi_o = \frac{Q_{i1}}{Q_{i2}} = 10\%$. For each xanthan concentration, different flow rate couples are tested with the flow rate of the continuous phase Q_{i2} ranging in between 50 mL/min and 500 mL/min.

By monitoring long sequences of flow images acquired for various driving flow rates and using solutions with different xanthan concentrations, several distinct dispersion modes are identified, Fig. 12. The images exemplified here are acquired within the visualization zone highlighted by a dashed line ellipse in Fig. 1(a). At low Reynolds numbers a parallel flow mode ("Mode 1") is observed, panel (a). This mode is observed when water and xanthan solutions are used as a continuous phase at very small flow rates. This mode is weakly unstable in the sense that the position of the interface between the fluids varies slowly in time. At larger Reynolds numbers, a second mode

("Mode 2") consisting of a thick filament of oil may be observed, panel (b). This second mode is not observed with pure water but only when xanthan is added to the continuous phase.

A third dispersion mode ("Mode 3") that may be observed consists of collection of thick filaments connected by branches, panel (c). A fourth mode ("Mode 4") we observe consists of thin filaments, panel (d). Like "Mode 2", this mode is solely observed when xanthan is added to the continuous phase. When the Reynolds number is increased even further, a fifth mode ("Mode 5") consisting of a collection of slugs and large oil drops may be observed. This mode is observed over the entire range of xanthan concentrations. Corresponding to the highest Reynolds numbers investigated, a mode consisting of small oil droplets ("Mode 6") is observed for both water and xanthan solutions.

By testing solutions with different xanthan concentrations at various driving flow rates, a chart of the dispersion modes is built, Fig. 13.

It is important to discuss the emergence of the various modes of dispersion in relation to the rheological behavior of the xanthan solutions.

The addition of xanthan gum leads to the emergence of three distinct dispersion modes ("Mode 2", "Mode 3" and "Mode 4") that are not observed when pure water is used as a continuous phase. This observation corroborates well with the strong and non-monotonic dependence of the mean diameter of the resulting emulsions on the xanthan concentration shown in Fig. 9.

It is interesting to discuss at this point the concentration bounds associated to the emergence of the modes solely observed when xanthan solutions are used. Thick filaments ("Mode 2") are observed solely for xanthan concentrations $C_{XG} \geq 0.05\%$. This concentration threshold closely matches the onset C^* of the semi-dilute rheological regime, Fig. 9.

Branched filaments are observed solely for $C_{XG} \geq 0.3\%$. This second threshold concentration closely matches the entanglement concentration C^e marking the yield stress rheological regime, Fig. 9. Equally interesting is the shape of the stability lines that separate various dispersion regimes. While the line separating the "Mode 1" from the "Mode 2" has a roughly monotonic shape, the stability lines separating "Mode 2" from "Mode 4", "Mode 4" from the "Mode 5" and "Mode 5" from "Mode 6" are clearly non-monotonic in xanthan concentration. The stability line separating "Mode 2" from "Mode 4" exhibits a local maximum roughly corresponding to $C_{XG} \approx C^{**} \approx 0.1\%$. The stability line separating "Mode 5" from "Mode 6" exhibits two local maxima: a first one at $C_{XG} \approx C^* \approx 0.05\%$ and a second one at $C_{XG} \approx C^e \approx 0.3\%$.

Particularly interesting is the emergence of "Mode 3". This mode is solely

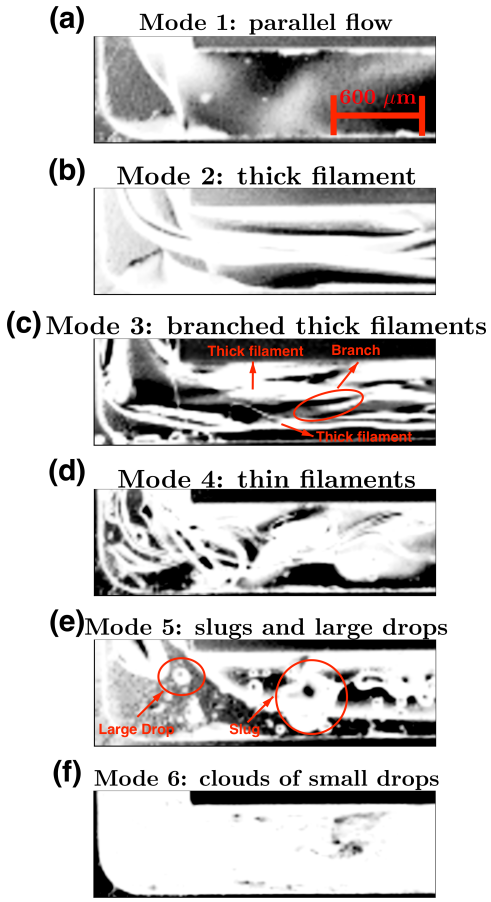

Figure 12: Illustration of various dispersion modes. Each flow image has been acquired within the region highlighted by an yellow ellipse in Fig. 1(a). The flow direction is from right to left.

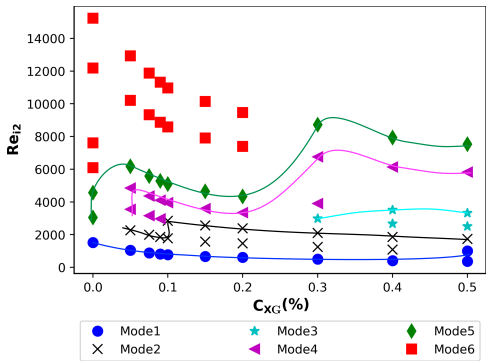

Figure 13: Dispersion modes of oil in water/xanthan solutions for different Reynolds numbers and concentrations of xanthan. The lines delineate the transitions between various dispersion regimes (see text for discussion).

observed for $C_{XG} \geq 0.3\%$ which corresponds to the yield stress rheological regime highlighted in Fig. 8. Bearing in mind that within this rheological regime the xanthan solutions exhibit a yield stress rheological behavior, the emergence of the branched filaments may be physically interpreted as follows. As the base flow below the onset of inertial turbulence is a Poiseuille flow it is reasonable to expect that, even in a turbulent state, the time averaged velocity gradients are the smallest around the centre-line of the micro-channel. Thus, it is likely to encounter material elements subjected to local stresses that are smaller than the yield stress and therefore in a solid state. As the branches between the filaments are systematically observed in the close vicinity of centre-line of the micro-channel (see panel (c) in Fig. 12), we associate them with solid bridges connecting the thick filaments.

We exemplify in Fig. 14 space time diagrams of the fluids' interface obtained with for a xanthan concentration $C_{XG} = 0.3\%$ in the continuous phase and several Reynolds numbers indicated in the top inserts. The space-time diagrams are built using a vertically oriented cut located in the middle of each frame of the image-sequence. We have purposely chosen the Reynolds numbers for the illustration in order to cover all the modes visually exemplified in Fig. 12. For the xanthan concentration we have chosen to illustrate in Fig. 14 it is clear that as the Reynolds number is increased, the complexity of the space-time dynamics of the flow patterns increases. Thus, as one moves from the rather basic "Mode 1" towards "Mode 6", an increasing number of characteristic space and time scales emerge.

We focus in the following on the analysis of the temporal correlations

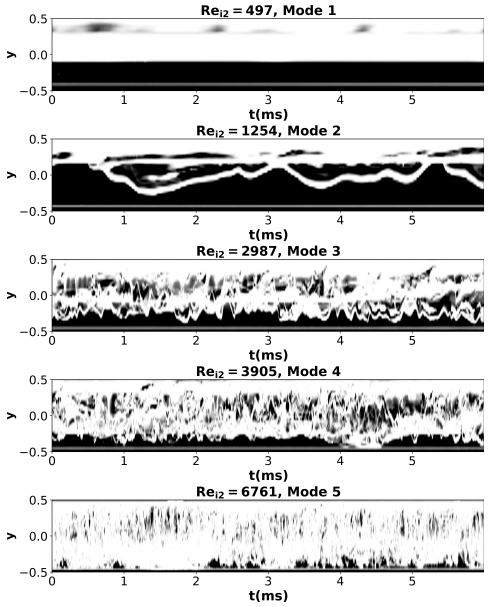

Figure 14: Space time diagrams computed for $C_x = 0.3\%$ xanthan in the continuous phase and several Reynolds numbers indicated in the top inserts. The dispersion modes are equally indicated in the top inserts.

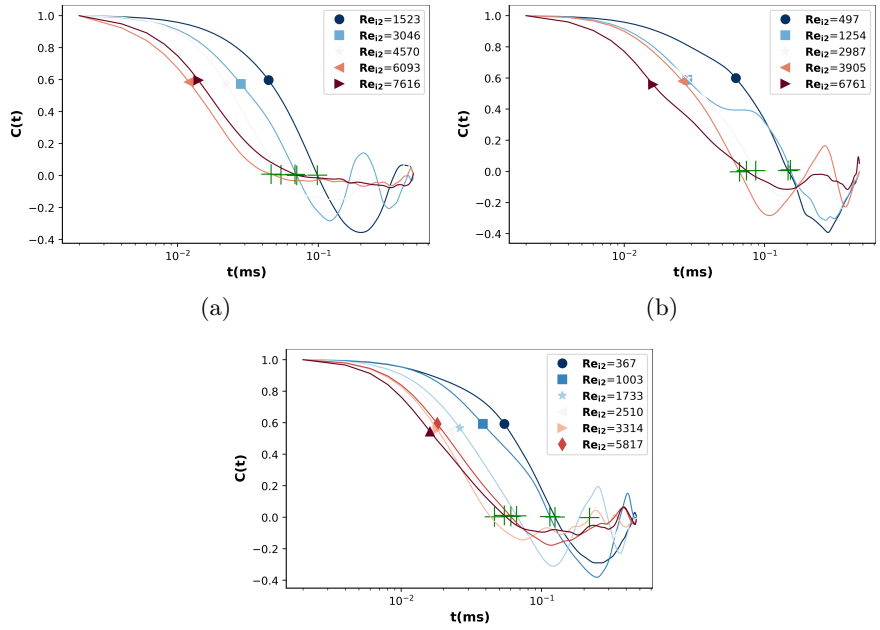

Figure 15: Example of time auto-correlation functions computed for several Reynolds numbers indicated in the inserts when three distinct fluids are used as continuous phase: (a) pure water ($C_{XG} = 0\%$) (b) xanthan solution with $C_{XG} = 0.2\%$ (c) xanthan solution with $C_{XG} = 0.5\%$. In each panel the plus markers indicate the zero-crossing of the correlation functions.

of the fluctuations of the interface. For this purpose we compute the time auto-correlation functions averaged within a band of width equal to 10% of the channel width and centered around the mid-point of the channel. Such time auto-correlation functions are exemplified in Fig. 15 for pure water (panel 15(a)), for a $C_{XG} = 0.2\%$ xanthan solution (panel 15(b)) and for a $C_{XG} = 0.5\%$ xanthan solution (panel 15(c)).

Regardless the xanthan concentration, at low Reynolds number the fluctuations of the interface between the fluids are strongly correlated in time (the data sets labelled by a circle in Fig. 15). As the Reynolds numbers are progressively increased past the onset of fully developed turbulent flow states, $Re_{i2} > 2300$, these fluctuations de-correlate.

The characteristic times of correlation of the fluctuations of the interfaces may be estimated by monitoring the zero-crossings of the time auto-correlation functions (see the "+" signs overlapped onto the data sets in Fig.

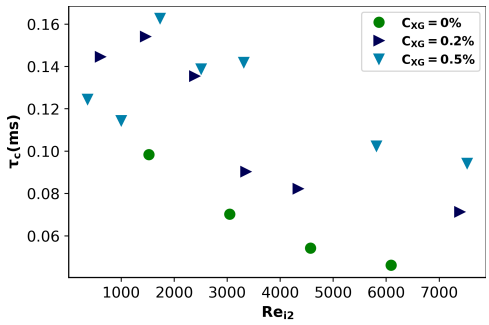

Figure 16: Dependence of the characteristic time of correlation of the interface fluctuations on the Reynolds number measured for three distinct xanthan concentrations detailed in the insert.

15), Fig. 16.

Past the onset of the fully developed turbulent regime ($Re_{i2} > 2300$) the characteristic correlation time decreases monotonically with the Reynolds number for each xanthan concentration. As the xanthan concentration is gradually increased, the correlation times measured within the turbulent flow regime increase. We associate this systematic increase of the level of correlations with the xanthan concentration with the emergence of the drag reduction phenomenon observed via the integral measurements presented in Sec. 3.2 which manifests at a local microscopic level through a *"laminarization"* of the flow.

Power spectra of the fluctuations of the interfaces computed using the same time series used for the calculation of time auto-correlation functions are shown in Fig. 17.

The large image acquisition frequency combined with the large number of flow images allow one to capture roughly four decades in the power of the velocity fluctuations spanning nearly two decades in frequency.

Within a transitional flow regime, $Re_{i2} \leq 2300$, the addition of xanthan results in the emergence of high frequency peaks (best visible for $C_{XG} = 0.5\%$ in panel 17(c)). According to the diagram of modes shown in Fig. 13, this corresponds to the emergence of the "Mode 2" for $C_{XG} = 0.2\%$ and of "Mode 2" and "Mode 3" for $C_{XG} = 0.5\%$.

Within the fully developed turbulent regime, $Re_{i2} > 2300$, three distinct scaling regimes are observed. In a range of low frequencies (or, according to the Taylor's frozen flow hypothesis, wave numbers) an inertial range roughly characterized by a $f^{-5/3}$ scaling is observed. In an intermediate range of frequencies, a steep $f^{-6.4}$ scaling consistent with a viscous spectral range is

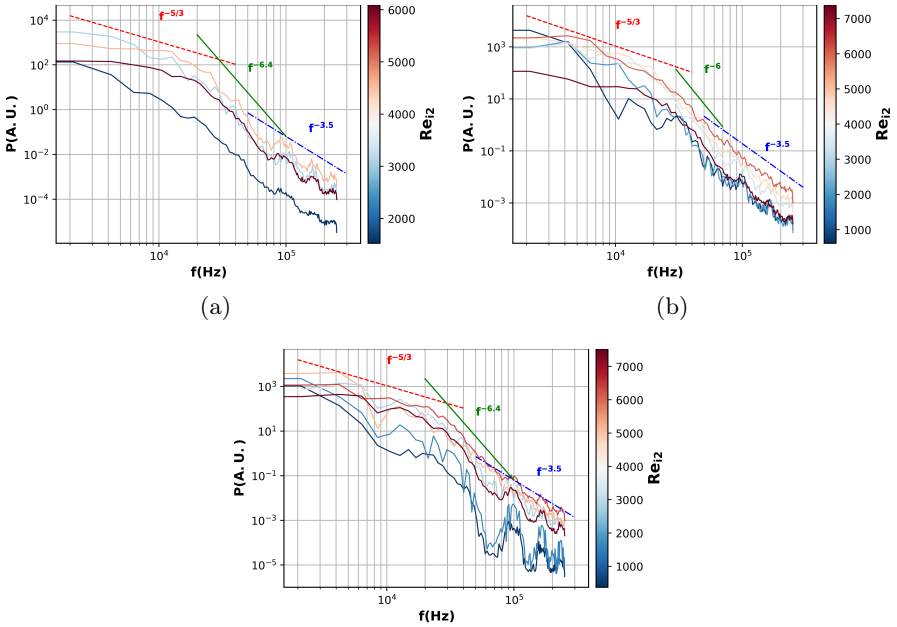

Figure 17: Example of power spectra of the interface fluctuations computed for several Reynolds numbers indicated in the inserts when three distinct fluids are used as continuous phase: (a) pure water ($C_{XG} = 0\%$) (b) xanthan solution with $C_{XG} = 0.2\%$ (c) xanthan solution with $C_{XG} = 0.5\%$. In each panel the values of the Reynolds number are mapped on the lateral color-bar. The lines are power law guides for the eye (see text for discussion).

observed. For the highest frequencies investigated, a $f^{-3.3}$ scaling consistent with a spatially smooth flow is observed. Last, it is interesting to compare the total vertical span of the spectra measured in a full developed turbulent regime when the xanthan concentration is increased. By a comparative analysis of the spectra presented in the top part of the panels 17(a), 17(b) and 17(c) of Fig. 17 (the data sets corresponding to the largest Re_{i2} investigated) it is clear that energy span covered by the spectra decreases upon the addition of xanthan. This indicates that the total energy associated to the turbulent velocity fluctuations decreases which is consistent with a *"laminarization"* of the flow associated to the drag reduction phenomenon.

3.4. Characterization of the flow fields

We focus in the following on the analysis of the turbulent flow fields that drive the microscopic emulsification process. As compared to the analysis of the dynamics of the interfaces detailed in the previous section, the measurements of the flow fields are performed in a limited range of flow rates and xanthan concentrations. These practical limitations mainly relate to the maximum frame rate of the camera. Time series of the velocity fields are measured during a total time of 50 ms which is comparable in magnitude to the viscous-inertial time scale and larger than the inertio-capillary time scale.

Time series of the velocity magnitude measured at the centre-line of the micro-channel measured for three distinct concentrations of xanthan and at a Reynolds number roughly chosen at the beginning of the fully developed turbulent regime are exemplified in Fig. 18(a). Each of the three time series exemplified exhibits *"slow"* (*i.e.* slower than the time averaged flow speed) intermittent events. To understand to role of the xanthan addition on the intermittent flow behavior, we plot in Fig. 18(b) the probability density functions of the reduced velocity fluctuations $\xi = \frac{U-U_{av}}{U^{rms}}$ for the same data sets illustrated in Fig. 18(a). Here $U_{av} = \langle U(t) \rangle_t$ is the time average of the velocity time series and $U^{rms} = \sqrt{\left\langle (U(t) - U_{av})^2 \right\rangle_t}$ is the root mean square (rms) of its fluctuations. While the right tails and the central parts of the pdf's which are well described by a Gaussian distribution are not affected by the xanthan addition, the left tails which follow an exponential scaling are systematically affected by it.

The dependence of the turbulence intensity defined as $I_t = \frac{U^{rms}}{U_{av}}$ measured at the centre-line of the micro-channel for three xanthan concentrations in the continuous phase is presented in Fig. 19.

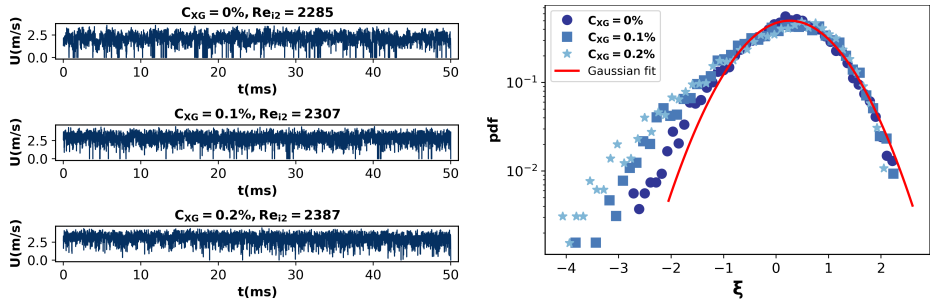

(a) (b)

Figure 18: (a) Illustration of velocity time series of the centre-line velocity measured with three distinct xanthan concentrations indicated in the top inserts. (b) Probability density functions (pdf's) of the centre-line velocity measured with three xanthan concentrations detailed in the insert. The full line is a Gaussian fitting function.

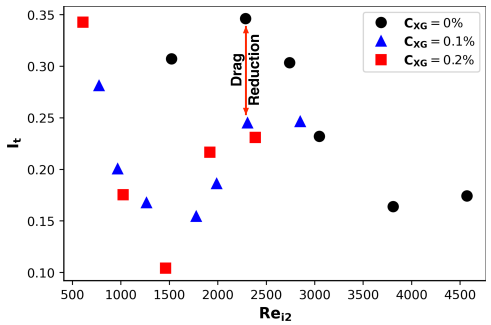

Figure 19: Dependence of the turbulence intensity (see text for definition) measured at the center line of the micro-channel on the Reynolds number for three xanthan concentrations detailed in the figure insert.

Regardless the xanthan concentration, the dependence of the turbulence intensity on the Reynolds number is non monotonic with an apparent local minimum in the beginning of the transitional flow regime $Re \approx 1500$ and a local maximum located around the onset of the fully developed regime. Such non-monotonic evolution of the turbulence intensity has been previously observed in macroscopic turbulent pipe flows of xanthan solutions, [52]. By comparing the different data sets displayed in Fig. 19 it is rather clear that, past the transitional flow regime, the xanthan addition leads to a significant decrease in the intensity of the turbulent states. We associate this observation as well with the emergence of the drag reduction phenomenon.

4. Conclusions and outlook

A systematic experimental study of emulsification of shear thinning fluids in inertially turbulent microscopic flows is presented. The central aim of the study is to understand the coupling between the ex-situ properties of the emulsions, the rheological regimes of the continuous phase, the hydrodynamic flow regimes, the dynamic modes of the emulsification process and the local properties of the flow fields.

To address this broad scope, the study combines several types of measurements: ex-situ measurements of the emulsions' granulometry, rheological characterization, integral flow measurements, local investigations of the dynamic modes of the emulsification and local measurements flow field.

The fluids used as continuous phase are aqueous solutions of xanthan with concentrations in the range $C_{XG} \in [0, 0.5](\%\text{wt})$. Within this broad range of concentrations four distinct rheological regimes of the xanthan solutions are observed, Fig. 8: dilute, semi-dilute, concentrated and entangled (yield stress). Whereas the first three rheological regimes are well documented in the literature, the yield stress behaviour of very concentrated xanthan solutions is much less understood. The granulometry of the emulsions obtained in turbulent flows at various Reynolds numbers and for various xanthan concentrations in the dispersed phase is strongly correlated to these rheological regimes, Fig. 9. Thus, corresponding to $C \approx C^{**}$ that marks the transition from the semi-dilute to the concentrated regime a peak of the dependence of the mean diameter of the emulsions is observed. A second change in the monotony of the trend of this dependence is observed at $C \approx C^{e}$ which marks the transition to a gel-like rheological behavior.

From a fluid mechanics point of view, the addition of xanthan to the continuous phase leads to the emergence of the drag reduction phenomenon

manifested through our experiments by an increase of the reduced flow resistance coefficient RFR, Fig. 11(a). The plateau value reached by the reduced flow resistance coefficient as the Reynolds number is increased increases with the xanthan concentration and the trend of this dependence changes at $C \approx C^{**}$ and $C \approx C^{e}$, Fig. 11(b) which indicates that the hydrodynamic regimes are also correlated with the rheological regimes.

The analysis of space-time dynamics of the interfaces between the continuous and the dispersed phase allowed one to provide a full mapping of the various emulsification modes observed within a wide range of Reynolds numbers and xanthan concentrations, Fig. 13.

Upon the addition of xanthan gum, three distinct dispersion modes (which are not observed when pure water is used as continuous phase) emerge: "Mode 2" - one thick filament, "Mode 3" - branched thick filaments and "Mode 4" - thin filaments. The separation lines between these new modes are equally related the rheological regimes of the continuous phase. The emergence of the drag reduction phenomenon significantly impacts both the local dynamic of the fluid interfaces and the local flow fields.

Thus, within the drag reduction regime, an increase in the level of correlations of the dynamics of the fluid interfaces is observed, Figs. 15, 16. The presence of the drag reduction leads to a decrease of the total span of the spectra of the fluctuations of the fluid interfaces, Fig. 17.

Though technically more limited than the measurements of the interfacial dynamics, the micro-PIV measurements of time series of the velocity fields revealed several important features triggered by the addition of xanthan to the continuous phase and the afore-mentioned emergence of the drag reduction. First, the emergence of the drag reduction strongly affects the intermittent behavior of the flow fields. Thus, upon the addition of xanthan the left-skewness of the probability density functions of the velocity fluctuations increases, Fig. 18. Within the drag reduction flow regime, a significant decrease of the level of fluctuations of the axial velocity measured at the centre-line of the micro-channel is observed, Fig. 19.

The central message of this experimental study is two-fold. From a practical perspective, the results reported herein open new avenues towards controlling the microscopic-scale emulsification process in a turbulent regime by fine rheological tuning of the continuous phase.

To sum up the interplay between the emulsification process and the drag reduction, we sketch in the operating diagram presented in Fig. 20 the efficient emulsification states assessed by a careful inspection of Fig. 9 (the gray highlighted region) and the drag reduction states (the blue highlighted region) that can be inferred from Fig. 11(a).

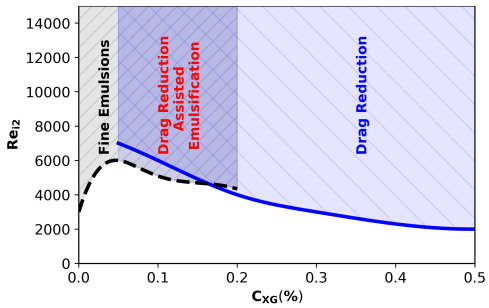

Figure 20: Sketch linking the efficient emulsification and drag reduction regimes. The black dashed line delineates the fine emulsification regime and the full line delineates the drag reduction regime. The shaded area highlight the relevant emulsification regimes (see text for discussion.)

The non monotonic dependence of the mean diameter of the emulsion combined with the emergence of the drag reduction phenomenon when a minute amount of xanthan is added to the continuous phase allows one to produce fine emulsions while keeping the energetic costs associated to the turbulent flow resistance within acceptable limits. The overlap regime visible in Fig. 11(a) is the regime of *"drag reduction assisted emuslification"* which, from a practical perspective, represents the main finding of this work.

From a fundamental standpoint, the addition of xanthan to the continuous phase adds several layers of complexity to the hydrodynamic problem. Thus, the panorama of dispersion modes is enriched with respect to the Newtonian emulsification case as a result of the presence of two sources of nonlinearity in the flow: inertial and rheological.

5. Acknowledgements

We gratefully acknowledge the support of the "Region Pays de la Loire", Chaire *Connect Talent ODE "Optical Diagnostics for Energy"*.

References

[1] C. Habchi, T. Lemenand, D. Della Valle, H. Peerhossaini, Liquid/liquid dispersion in a chaotic advection flow, International Journal of Multiphase Flow 35 (2009) 485–497.

[2] T. Lemenand, C. Habchi, D. Della Valle, J. Bellettre, H. Peerhossaini, Mass transfer and emulsification by chaotic advec-

tion, International Journal of Heat and Mass Transfer 71 (2014) 228–235. URL: https://www.sciencedirect.com/science/article/pii/S0017931013010594. doi:https://doi.org/10.1016/j.ijheatmasstransfer.2013.12.015.

[3] N. Vankova, S. Tcholakova, N. D. Denkov, I. B. Ivanov, V. D. Vulchev, T. Danner, Emulsification in turbulent flow: 1. mean and maximum drop diameters in inertial and viscous regimes, Journal of Colloid and Interface Science 312 (2007) 363–380. URL: https://www.sciencedirect.com/science/article/pii/S0021979707003803. doi:https://doi.org/10.1016/j.jcis.2007.03.059.

[4] A. Montillet, S. Nedjar, M. Tazerout, Continuous production of water-in-oil emulsion using micromixers, Fuel 106 (2013) 410–416. URL: https://www.sciencedirect.com/science/article/pii/S0016236112008940. doi:https://doi.org/10.1016/j.fuel.2012.11.018.

[5] A. Tamir, S. Sobhi, A new two-impinging-streams emulsifier, AIChE Journal 31 (1985) 2089–2092. URL: https://aiche.onlinelibrary.wiley.com/doi/abs/10.1002/aic.690311221. doi:https://doi.org/10.1002/aic.690311221. arXiv:https://aiche.onlinelibrary.wiley.com/doi/pdf/10.1002/aic.690311221.

[6] T. Kiljański, Preparation of emulsions using impinging streams, AIChE Journal 50 (2004) 1636–1639. URL: https://aiche.onlinelibrary.wiley.com/doi/abs/10.1002/aic.10155. doi:https://doi.org/10.1002/aic.10155. arXiv:https://aiche.onlinelibrary.wiley.com/doi/pdf/10.1002/aic.10155.

[7] N. Mouheb, A. Montillet, C. Solliec, J. Havlica, P. Legentilhomme, J. Comiti, J. Tihon, Flow characterization in t-shaped and cross-shaped micromixers, Microfluidics and Nanofluidics 10 (2011) 1185–1197. doi:10.1007/s10404-010-0746-5.

[8] D. Tsaoulidis, P. Angeli, Liquid-liquid dispersions in intensified impinging-jets cells, Chemical Engineering Science 171 (2017) 149–159. URL: https://www.sciencedirect.com/science/article/pii/S0009250917303287. doi:https://doi.org/10.1016/j.ces.2017.05.016.

[9] A. Belkadi, D. Tarlet, A. Montillet, J. Bellettre, P. Massoli, Water-in-oil emulsification in a microfluidic impinging flow at high capillary numbers, International Journal of Multiphase Flow 72 (2015) 11–23. URL: https://www.sciencedirect.com/science/article/pii/S0301932215000178. doi:https://doi.org/10.1016/j.ijmultiphaseflow.2015.01.007.

[10] A. Belkadi, D. Tarlet, A. Montillet, J. Bellettre, P. Massoli, Study of two impinging flow microsystems arranged in series. application to emulsified biofuel production, Fuel 170 (2016) 185–196. doi:10.1016/j.fuel.2015.12.025.

[11] Y. Ji, J. Bellettre, A. Montillet, P. Massoli, Fast oil-in-water emulsification in microchannel using head-on impinging configuration: Effect of swirl motion, International Journal of Multiphase Flow 131 (2020) 103402.

[12] J. Husny, J. J. Cooper-White, The effect of elasticity on drop creation in t-shaped microchannels, Journal of Non-Newtonian Fluid Mechanics 137 (2006) 121–136. URL: https://www.sciencedirect.com/science/article/pii/S0377025706000796. doi:https://doi.org/10.1016/j.jnnfm.2006.03.007, extensional Flow.

[13] P. E. Arratia, J. P. Gollub, D. J. Durian, Polymeric filament thinning and breakup in microchannels, Phys. Rev. E 77 (2008) 036309. URL: https://link.aps.org/doi/10.1103/PhysRevE.77.036309. doi:10.1103/PhysRevE.77.036309.

[14] P. E. Arratia, L.-A. Cramer, J. P. Gollub, D. J. Durian, The effects of polymer molecular weight on filament thinning and drop breakup in microchannels, New Journal of Physics 11 (2009) 115006. URL: https://doi.org/10.1088/1367-2630/11/11/115006. doi:10.1088/1367-2630/11/11/115006.

[15] L. Derzsi, M. Kasprzyk, J. P. Plog, P. Garstecki, Flow focusing with viscoelastic liquids, Physics of Fluids 25 (2013) 092001. URL: https://doi.org/10.1063/1.4817995. doi:10.1063/1.4817995. arXiv:https://doi.org/10.1063/1.4817995.

[16] E. Chiarello, L. Derzsi, M. Pierno, G. Mistura, E. Piccin, Generation of oil droplets in a non-newtonian liquid using a microfluidic

t-junction, Micromachines 6 (2015) 1825–1835. URL: https://www.mdpi.com/2072-666X/6/12/1458. doi:10.3390/mi6121458.

[17] G. F. Christopher, S. L. Anna, Passive breakup of viscoelastic droplets and filament self-thinning at a microfluidic t-junction, Journal of Rheology 53 (2009) 663–683. URL: https://doi.org/10.1122/1.3086871. doi:10.1122/1.3086871. arXiv:https://doi.org/10.1122/1.3086871.

[18] C.-X. Zhao, A. P. Middelberg, Two-phase microfluidic flows, Chemical Engineering Science 66 (2011) 1394–1411.

[19] V. Krstonošić, L. Dokić, I. Nikolić, M. Milanović, Influence of xanthan gum on oil-in-water emulsion characteristics stabilized by osa starch, Food Hydrocolloids 45 (2015) 9–17. URL: https://www.sciencedirect.com/science/article/pii/S0268005X14003968. doi:https://doi.org/10.1016/j.foodhyd.2014.10.024.

[20] Investigation on the Droplet Formation Time With Xanthan Gum Solutions at a T-Junction, volume Volume 2 of *Fluids Engineering Division Summer Meeting*, 2012. URL: https://doi.org/10.1115/FEDSM2012-72133. doi:10.1115/FEDSM2012-72133.

[21] K. Shimizu, K. Minekawa, T. Hirose, Y. Kawase, Drop breakage in stirred tanks with newtonian and non-newtonian fluid systems, Chemical Engineering Journal 72 (1999) 117–124. URL: https://www.sciencedirect.com/science/article/pii/S1385894798001508. doi:https://doi.org/10.1016/S1385-8947(98)00150-8.

[22] B. A. Toms, Some observations on the flow of linear polymer solutions through straight tubes at large reynolds numbers, Proc. First Int. Conger. on Rheology 2 (1949) 135–141.

[23] Y. Ji, E. Missi, J. Bellettre, T. Burghelea, A. Montillet, P. Massoli, Dynamics of a newtonian droplet in the turbulent flow of a shear thinning fluid in a microchannel, Phys. Rev. Fluids 8 (2023) 043301. URL: https://link.aps.org/doi/10.1103/PhysRevFluids.8.043301. doi:10.1103/PhysRevFluids.8.043301.

[24] R. Lopes, R. O. Rodrigues, D. Pinho, V. Garcia, H. Schütte, R. Lima, S. Gassmann, Low cost microfluidic device for partial cell separation: Micromilling approach, in: 2015 IEEE International Conference on

Industrial Technology (ICIT), 2015, pp. 3347–3350. doi:10.1109/ICIT.2015.7125594.

[25] Y. Ji, J. Bellettre, A. Montillet, P. Massoli, Experimental investigation on single drop breakage in two-stream impinging microchannels, Experiments in Fluids 62 (2021) 17. URL: https://doi.org/10.1007/s00348-020-03124-0. doi:10.1007/s00348-020-03124-0.

[26] A. Liberzon, D. Lasagna, M. Aubert, P. Bachant, T. Käufer, jakirkham, A. Bauer, B. Vodenicharski, C. Dallas, J. Borg, et al., Openpiv/openpiv-python: Openpiv - python (v0.22.2) with a new extended search piv grid option (2020). doi:10.5281/zenodo.3930343.

[27] G. Sworn, Handbook of hydrocolloids, Boca Raton, Fla., 2009, pp. 186–203.

[28] A. Roy, Synthèse et caractérisation de dérivés amphiphiles du xanthane, Ph.D. thesis, Université du Havre, 2015.

[29] G. Van Aken, Food polysaccharides and their applications. 2nd ed., Boca Raton, FL: CRC/Taylor & Francis, 2009, p. 521–539.

[30] A. Rodd, D. Dunstan, D. Boger, Characterisation of xanthan gum solutions using dynamic light scattering and rheology, Carbohydrate Polymers 42 (2000) 159–174. URL: https://www.sciencedirect.com/science/article/pii/S0144861799001563. doi:https://doi.org/10.1016/S0144-8617(99)00156-3.

[31] D. J. McClements, Food emulsions: principles, practices, and techniques. 2. ed., Boca Raton, Fla.: CRC Press;, 2005, p. 609.

[32] C. J. Pipe, T. S. Majmudar, G. H. McKinley, High shear rate viscometry, Rheologica Acta 47 (2008) 621–642. URL: https://doi.org/10.1007/s00397-008-0268-1. doi:10.1007/s00397-008-0268-1.

[33] J. Sepulveda, A. Montillet, D. D. Valle, T. Amiar, H. Ranchon, C. Loisel, A. Riaublanc, Experimental determination and modeling of flow curves of xanthan gum solutions over a large range of shear rates, Applied Rheology 31 (2021) 24–38. URL: https://doi.org/10.1515/arh-2020-0116. doi:doi:10.1515/arh-2020-0116.

[34] V. Carnicer, C. Alcàzar, M. Orts, E. Sánchez, R. Moreno, Microfluidic rheology: A new approach to measure viscosity of ceramic suspensions at extremely high shear rates, Open Ceramics

5 (2021) 100052. URL: https://www.sciencedirect.com/science/article/pii/S2666539520300523. doi:https://doi.org/10.1016/j.oceram.2020.100052.

[35] P. Guillot, P. Panizza, J.-B. Salmon, M. Joanicot, A. Colin, C.-H. Bruneau, T. Colin, Viscosimeter on a microfluidic chip, Langmuir 22 (2006) 6438–6445. URL: https://doi.org/10.1021/la060131z. doi:10.1021/la060131z. arXiv:https://doi.org/10.1021/la060131z, pMID: 16800711.

[36] P. Nghe, E. Terriac, M. Schneider, Z. Z. Li, M. Cloitre, B. Abecassis, P. Tabeling, Microfluidics and complex fluids, Lab Chip 11 (2011) 788–794. URL: http://dx.doi.org/10.1039/C0LC00192A. doi:10.1039/C0LC00192A.

[37] C. W. Macosko, Rheology: principles, measurements, and applications, Wiley, New York, 1994.

[38] C. Miller, Predicting non-newtonian flow behavior in ducts of unusual cross section, Industrial & Engineering Chemistry Fundamentals 11 (1972) 524–528. URL: https://doi.org/10.1021/i160044a015. doi:10.1021/i160044a015. arXiv:https://doi.org/10.1021/i160044a015.

[39] P. Coussot, Rheometry of pastes, suspensions and granular materials, John Willey & Sons, 2005.

[40] E. E. S. Ong, S. O'Byrne, J. L. Liow, Yield stress measurement of a thixotropic colloid, Rheologica Acta 58 (2019) 383–401. URL: https://doi.org/10.1007/s00397-019-01154-y. doi:10.1007/s00397-019-01154-y.

[41] N. B. Wyatt, M. W. Liberatore, Rheology and viscosity scaling of the polyelectrolyte xanthan gum, Journal of Applied Polymer Science 114 (2009) 4076–4084. URL: https://onlinelibrary.wiley.com/doi/abs/10.1002/app.31093. doi:https://doi.org/10.1002/app.31093. arXiv:https://onlinelibrary.wiley.com/doi/pdf/10.1002/app.31093.

[42] E. M. Nsengiyumva, P. Alexandridis, Xanthan gum in aqueous solutions: Fundamentals and applications, International Journal of Biological Macromolecules 216 (2022) 583–604.

[43] J. Lachaise, B. Mendiboure, C. Dicharry, G. Marion, M. Bourrel, P. Cheneviere, J. Salager, A simulation of emulsification by turbulent stirring, Colloids and Surfaces A: Physicochemical and Engineering Aspects 94 (1995) 189–195. URL: https://www.sciencedirect.com/science/article/pii/0927775794029784. doi:https://doi.org/10.1016/0927-7757(94)02978-4.

[44] A. A. Pena, Dynamic aspects of emulsion stability, Rice University, 2004.

[45] W. R. dos Santos, E. Spalenza Caser, E. J. Soares, R. N. Siqueira, Drag reduction in turbulent flows by diutan gum: A very stable natural drag reducer, Journal of Non-Newtonian Fluid Mechanics 276 (2020) 104223.

[46] A. S. Pereira, R. M. Andrade, E. J. Soares, Drag reduction induced by flexible and rigid molecules in a turbulent flow into a rotating cylindrical double gap device: Comparison between poly (ethylene oxide), polyacrylamide, and xanthan gum, Journal of Non-Newtonian Fluid Mechanics 202 (2013) 72–87. URL: https://www.sciencedirect.com/science/article/pii/S037702571300178X. doi:https://doi.org/10.1016/j.jnnfm.2013.09.008.

[47] R. S. Mitishita, G. J. Elfring, I. A. Frigaard, Statistics and spectral analysis of turbulent duct flows with flexible and rigid polymer solutions, Journal of Non-Newtonian Fluid Mechanics 311 (2023) 104952. URL: https://www.sciencedirect.com/science/article/pii/S0377025722001719. doi:https://doi.org/10.1016/j.jnnfm.2022.104952.

[48] Y. Zhao, G. Chen, Q. Yuan, Liquid-liquid two-phase flow patterns in a rectangular microchannel, AIChE Journal 52 (2006) 4052–4060. URL: https://aiche.onlinelibrary.wiley.com/doi/abs/10.1002/aic.11029. doi:https://doi.org/10.1002/aic.11029. arXiv:https://aiche.onlinelibrary.wiley.com/doi/pdf/10.1002/aic.11029.

[49] M. Kashid, L. Kiwi-Minsker, Quantitative prediction of flow patterns in liquid–liquid flow in micro-capillaries, Chemical Engineering and Processing: Process Intensification 50 (2011) 972–978. URL: https://www.sciencedirect.com/science/article/pii/S0255270111001553. doi:https://doi.org/10.1016/j.cep.2011.07.003.

[50] D. Tsaoulidis, V. Dore, P. Angeli, N. V. Plechkova, K. R. Seddon, Flow patterns and pressure drop of ionic liquid–water two-phase flows in microchannels, International Journal of Multiphase Flow 54 (2013) 1–10. URL: https://www.sciencedirect.com/science/article/pii/S0301932213000323. doi:https://doi.org/10.1016/j.ijmultiphaseflow.2013.02.002.

[51] O. Der, V. Bertola, An experimental investigation of oil-water flow in a serpentine channel, International Journal of Multiphase Flow 129 (2020) 103327. URL: https://www.sciencedirect.com/science/article/pii/S0301932219308444. doi:https://doi.org/10.1016/j.ijmultiphaseflow.2020.103327.

[52] B. Güzel, T. Burghelea, I. A. Frigaard, D. M. Martinez, Observation of laminar-turbulent transition of a yield stress fluid in hagen-poiseuille flow, Journal of Fluid Mechanics 627 (2009) 97–128.